SCIREA Journal of Physics
ISSN: 2706-8862
http://www.scirea.org/journal/Physics
August 5, 2025
Volume 10, Issue 4, August 2025
https://doi.org/10.54647/physics140693

Adaptation of a Diagnostic X-Ray Digital Flat Panel Detector for Treatment Verification of a Telecobalt Machine

Victoria Nketia[1], Mark Pokoo-Aikins[1,2], Samuel Nii Tagoe[1,3], Francis Hasford[1,2],Theresa Bebaaku Dery[1,2], John Boham Noonoo[4], Bismark Djan[5]

[1] Medical Physics Department, Graduate School of Nuclear and Allied Sciences, University of Ghana, P.O. Box AE 1, Accra-Ghana

[2] Radiological and Medical Sciences Research Institute, Ghana Atomic Energy Commission, P.O. Box LG 80, Accra, Ghana.

[3] National Center for Radiotherapy and Nuclear Medicine Korle Bu Teaching Hospital, Accra, Ghana

[4] University of Ghana Medical Center Radiology Department, P. O. Box LG 25, Accra, Ghana

[5] Radiation Protection Institute Ghana Atomic Energy Commission, P. O. Box LG 80, Accra, Ghana

Abstract

Portal imaging devices, such as flat panel detectors (FPDs), have largely replaced traditional films in radiation therapy due to their ability to provide real-time imaging and digital storage. However, telecobalt machines are typically not equipped with such imaging systems, requiring the continued use of films for patient position verification. This reliance on film introduces cost implications and delays in treatment due to the time-consuming nature of film processing. This study explores the feasibility of adapting a diagnostic flat panel detector for portal imaging in a telecobalt machine. An in-house water phantom embedded with test objects was constructed to evaluate image quality. Image quality metrics, including signal-to-noise ratio (SNR), contrast-to-noise ratio (CNR), and resolution using bar patterns, were assessed across various regions of interest. The detector software required predefined diagnostic X-ray exposure parameters, which could not be manually adjusted. Image quality was evaluated using various preset protocols, with analysis performed in ImageJ. Optimal image quality was achieved

with the "Skull Lat" protocol (70 kVp, 8 mAs). However, for improved visualization of soft tissue, the "Right Clavicle AP" protocol (65 kVp, 16 mAs) is recommended. The findings demonstrate that a diagnostic flat panel detector can be effectively adapted for patient position verification in telecobalt treatments, enhancing treatment accuracy and patient safety.

Keywords: Patient Position Verification, Flat Panel Detector, Telecobalt Machine, Image Quality

Introduction

The success of radiotherapy depends critically on the accurate delivery of the prescribed dose to the tumor while minimizing exposure to surrounding healthy tissues (Bacher et al., 2003). Ensuring that the patient's position during treatment matches the planned setup is essential for maintaining this accuracy. Treatment verification is therefore a key quality assurance component in radiation therapy, helping to detect and correct potential errors during patient setup and beam delivery (Ebert et al., 2018).

Several techniques have been developed to support treatment verification, including electronic portal imaging devices (EPIDs) and cone-beam computed tomography (IAEA Human Health Report, 2013). EPIDs have largely replaced film-based systems due to their ability to provide real-time digital images and improved workflow efficiency. These devices use a megavoltage beam to acquire projection images during treatment, allowing for the evaluation of patient positioning and beam alignment (Elmpt et al., 2008).

Flat panel detectors, a common type of EPID, offer advantages such as compact design, real-time image display, and the ability to store images digitally for archiving or review (Tsutomu et al., 2006; Khan & Gibbons, 2014). Despite these benefits, telecobalt therapy units-still widely used in some resource-limited settings—are not typically equipped with such portal imaging systems. This study investigates the feasibility of adapting a diagnostic flat panel detector for patient position verification on a telecobalt unit for viewing or archiving (Khan & Gibbons, 2014).

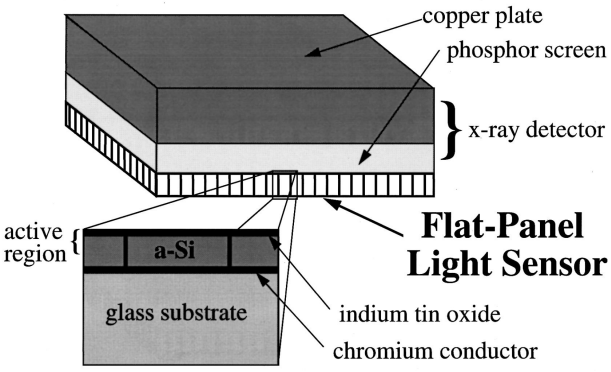

Figure 1: *Schematic diagram of the a-Si PID (Source: AAPM TG58 Manual)*

Figure 1 shows a schematic diagram of the electronic portal imaging device (EPID). Although the number of operational modes varies across commercial EPIDs, the most common functionalities include real-time imaging, dose verification, and patient setup verification (Herman et al., 2001). Certain treatment geometries-such as total-body irradiation-require dosimetric verification, often achieved through in vivo dosimetry (IVD). IVD involves radiation measurements taken during treatment and provides information about the absorbed dose within the patient (Dieterich et al., 2016). Therefore, an effective IVD system must be capable of detecting issues such as equipment malfunctions, dose calculation errors, patient misalignment, and anatomical changes (Olaciregui-Ruiz et al., 2020).

This study was conducted at the **National Center for Radiotherapy and Nuclear Medicine (NCRNM)** at **Korle-Bu Teaching Hospital**, where a **telecobalt therapy unit** is still in clinical use. Unlike modern linear accelerators, telecobalt machines typically lack built-in portal imaging systems. As a result, clinicians at the center rely on radiographic films for treatment verification. This practice poses several challenges, including high costs associated with film and chemical procurement, delays due to film processing time, and the lack of real-time feedback required for on-the-spot patient positioning adjustments. Additionally, the film processor at the center is outdated and no longer reliable, which further complicates the verification process. In response to these limitations, the center has recently acquired a **diagnostic flat panel detector** intended for integration with the telecobalt unit to enable digital verification imaging. **The objective of this study** was to evaluate the performance of this diagnostic radiography flat panel detector when used as a patient position verification tool for the telecobalt unit at NCRNM. The goal is to determine its suitability for clinical implementation in a resource-limited setting.

Materials and Methods

Construction of the Phantom

A tissue-equivalent phantom was constructed using **Perspex (polymethyl methacrylate, PMMA)** to simulate anatomical structures in the thoracic region. The phantom measured **30 cm × 20 cm** in area and was fabricated from 1 cm-thick Perspex sheets. Embedded within the phantom were materials with varying densities - **Styrofoam**, **aluminum**, and **lead** - to simulate soft tissue, bone, and high-density structures, respectively, and to enhance contrast for image quality evaluation.

The individual Perspex sheets were chemically bonded using **chloroform (trichloromethane)**, a solvent known to dissolve PMMA, ensuring a tight seal between components. An **inlet and outlet** system was incorporated to allow the phantom to be filled with water, which further enhanced tissue equivalence and mimicked the scattering and attenuation properties of human tissue. A **leakage test** was performed to ensure watertight integrity.

To assess image quality, **step wedges** composed of Styrofoam (low contrast) and lead (high contrast) were positioned on opposite sides of the phantom. These were used to calculate **signal-to-noise ratio (SNR)** and **contrast-to-noise ratio (CNR)**. Additionally, resolution testing was conducted using aluminum bar patterns with **thicknesses of 1 mm, 2 mm, and 3 mm**, arranged within the phantom to determine the system's spatial resolution

capability. The overall thickness and design of the phantom were intended to approximate the anatomical dimensions and imaging challenges of the human thorax.

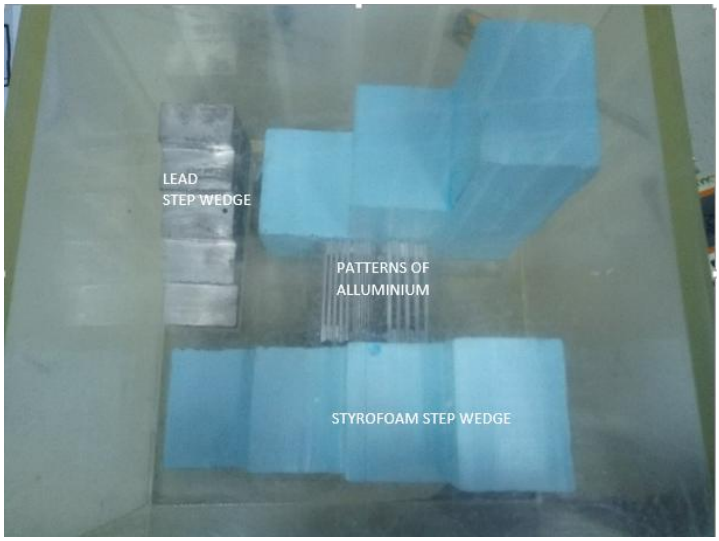

Figure 2: *A picture of the arrangement of Aluminium sheet of different thickness, Styrofoam and Lead in the phantom.*

Treatment Setup

All radiation measurements in this study were carried out using a **Theratron Equinox-100 cobalt-60 teletherapy machine** retrofitted with a flat panel detector at the National Center for Radiotherapy and Nuclear Medicine. The phantom was placed on the treatment couch using a **source-to-image distance (SID)** technique of **120 cm**, and the **source-to-phantom distance** was maintained at **87 cm**, as illustrated in Figure 3.

The flat panel detector was mounted on a mobile stand and positioned beneath the treatment couch, and aligned such that the source-to-detector distance was also 120 cm. The detector consisted of an image acquisition unit with an active image area of **430 × 430 mm² (17 × 17 inches)**, physical dimensions of **460 × 460 × 16 mm³**, and an image matrix of **3040 × 3036 pixels**. It offered a spatial resolution of **3.7-line pairs per millimeter (lp/mm)** and supported **16-bit grayscale imaging**. These specifications ensured high-resolution image acquisition suitable for patient positional verification under telecobalt irradiation conditions

Image Acquisition

All images were acquired in integrated mode using the flat panel detector (FPD) system in conjunction with the Theratron Equinox 100 cobalt-60 teletherapy machine, operated through the Digital Radiography Operating Console (DROC) software. This system enabled synchronization

between the detector and the telecobalt unit, allowing the acquisition of two-dimensional images within seconds following irradiation. All portal images were saved in DICOM format.

During image acquisition, the detector was positioned beneath the treatment couch and aligned at the central axis of the radiation beam, replicating patient treatment conditions. The Digital Radiography Console was used to select predefined imaging protocols, which included labels corresponding to various kVp and mAs settings. The corresponding parameters for each protocol are presented in Table 1.

Image analysis was performed using ImageJ, a Java-based image processing software, and Microsoft Excel. Regions of interest (ROIs) were identified and labeled within ImageJ to facilitate the quantitative assessment of image quality metrics.

Table 1: Assigned Imaging Protocols for Various Sections

Assigned Label	Description	kV	mAs
A1	Zygomatic arche	65	4
A2	Stenvers view	75	20
A3	Skull PA Axial	75	16
A4	Skull LAT, right	70	8
A5	Sinuses, water	80	32
A6	Sella Turcica	70	12.5
A7	Orbit PA	70	16
A8	Nasal Bone LAT, right	50	2.5
B1	Sternum OBL, left anterior	60	8
B2	Sternum LAT, right	80	12.5
B3	Right clavicle AP Axial	75	12.5
B4	Right clavicle AP	65	16
B5	Rib PA	65	10
B6	Chest PA	120	2.5
B7	Chest LAT, right	120	8
C1	T-Spine LAT, right	80	40

C2	T-Spine AP	75	64
C3	Sacrum LAT, left	85	64
C4	Sacrum AP	75	32
C5	L Spine OBL, left	75	25
C6	L Spine LAT, right	90	25
C7	L Spine AP	80	20
C8	Coccyx LAT, left	85	64
C9	C-Spine OBL, right	65	5
C10	Coccyx AP	75	20
D1	Pelvis LAT, right	90	64
D2	Pelvis AP	70	16
D3	IVP9	75	8
D4	Abdomen LAT, right	80	10
D5	Abdomen AP, supine	75	16
E1	Right wrist PA	50	2
E2	Right Shoulder Transaxillary	65	5
E3	Right shoulder AP	65	12.5
E4	Right Shoulder Scapula LAT	70	12.5
E5	Right Scapula AP	70	6.3
E6	Right elbow AP	50	2.5
F1	Left Toe OBL	50	2.5
F2	Left Tibia LAT	60	1.6
F3	Left Patella Tangential	60	40
F4	Left Patella AP	60	2
F5	Left Hip LAT	70	16
F6	Left foot OBL	50	6.3
F7	Left foot LAT, standing	50	4
F8	Left foot LAT	50	5
F9	Left femur LAT	70	16

A - Head, B - Thorax, C - Spine, D - Abdomen, E - Arm and F - Leg

Assessment of Quality of Images

The images were taken for a variety of examinations on various parts of the body on the DROC software that comes with the flat panel detector at a treatment time of 0.1 minute. Image J software was used to analyze image quality. The images were evaluated using image J software.

Figures 4 and 5 show how regions of interest (ROI) were determined on each of the Styrofoam and lead step wedges designs, as well as a backdrop ROI, utilizing photos of the created phantom. The image J software was used to calculate the mean gray levels and standard deviation for each of the steps.

For evaluation of the image quality of the images obtained from the FPD, signal to noise ratio (SNR), contrast to noise ratio (CNR), and resolution were the metrics studied.

The following formula was used to obtain the signal to noise ratio.

$$SNR = \left|\frac{S1_{Mean}|}{\sqrt{SD}}\right| \ldots\ldots\ldots\ldots\ldots\ldots\ldots \quad 1$$

where $S1_{Mean}$ is the mean pixel value over the region of interest in both the high contrast region and low contrast region and SD is the standard deviation of the pixel values.

The following formula was used to obtain the contrast to noise ratio.

$$CNR = \frac{|S1_{Mean} - S2_{mean}|}{\sqrt{(SD_{ROI})^2 - (SD_B)^2}} \ldots\ldots\ldots\ldots\ldots\ldots 2$$

where $S1_{Mean}$ is the mean pixel value over the region of interest in both the high contrast region and low contrast region whiles $S2_{mean}$ is the background region's average pixel value SD_{ROI} is the standard deviation of pixel values, while SD_B is the standard deviation of background pixel value.

Results and Discussion

Results for Signal-to-noise and contrast-to-noise ratios in the low and high-contrast regions are shown in Tables 2 and 3 respectively.

Table 2: SNR and CNR values for the irradiated phantom using the FPD.

Assigned Label	SNR for High Contrast Region					CNR for High Contrast Region					Fitted Line Gradient
	1	2	3	4	5	1	2	3	4	5	
A1	264.06	188.15	158.20	131.65	106.98	9.35	5.99	4.60	3.38	2.05	22.33
A2	240.39	202.34	190.65	151.38	120.93	12.33	9.42	8.75	6.20	4.41	3.02
A3	292.79	240.69	226.59	176.71	138.38	16.54	12.11	11.14	7.57	5.27	17.14
A4	537.42	440.31	413.24	318.94	243.79	18.40	16.11	15.05	11.06	6.93	25.98
A5	314.77	239.56	224.39	174.00	132.47	18.01	11.91	10.92	7.47	4.94	20.70
A6	362.12	280.51	262.20	223.76	189.44	7.80	6.06	5.42	4.05	2.51	26.67
A7	314.21	239.15	228.46	178.69	137.64	18.59	12.11	11.49	7.93	5.36	19.80
A8	422.99	319.38	299.32	240.57	185.88	15.94	12.23	11.09	8.05	5.00	28.38
B1	860.53	590.57	540.97	439.28	341.49	10.24	9.42	8.93	7.49	5.14	20.45
B2	951.92	632.52	590.09	488.75	381.91	10.59	9.68	9.23	7.83	5.46	16.84
B3	846.32	586.93	533.70	427.00	333.81	9.28	8.60	8.16	6.82	4.72	21.54
B4	504.14	365.95	313.35	247.68	189.66	8.11	7.12	6.29	4.74	2.84	45.83
B5	376.44	321.39	320.17	296.79	272.88	7.14	5.64	5.28	4.24	2.81	7.18
B6	380.10	317.44	316.05	285.91	263.36	10.74	8.14	7.69	6.08	4.22	6.70

B7	964.14	646.39	601.41	492.43	383.76	10.79	9.91	9.47	7.99	5.56	16.78
C1	461.91	317.40	346.44	282.79	232.05	19.13	12.13	13.42	9.68	6.47	17.79
C2	404.06	283.15	316.56	261.16	218.85	16.32	9.88	11.43	8.15	5.47	13.82
C3	442.94	311.18	325.47	260.37	208.49	15.22	10.63	10.93	7.82	5.04	25.46
C4	401.11	293.29	309.72	255.26	217.45	14.66	9.92	10.40	7.51	5.17	16.04
C5	455.99	318.70	341.83	278.52	222.88	17.50	11.70	12.54	9.11	5.87	20.62
C6	457.15	318.35	344.12	279.39	228.05	17.75	11.74	12.72	9.17	6.09	19.15
C7	258.05	228.87	199.70	169.95	148.70	6.28	5.37	4.32	3.08	1.83	19.11
C8	473.26	322.68	349.36	284.07	229.03	19.10	12.25	13.36	9.62	6.24	19.78
C9	285.25	233.45	217.01	196.61	178.51	6.92	5.19	4.45	3.47	2.31	12.06
C10	414.30	298.27	322.33	267.21	227.69	23.67	12.30	14.36	9.74	6.63	13.86
D1	343.65	283.63	259.69	223.76	191.65	8.12	6.60	5.73	4.37	2.85	23.63
D2	1051.94	783.09	793.70	659.42	550.39	11.48	10.20	9.84	8.18	5.86	7.65
D3	334.13	259.23	251.48	218.34	192.01	10.93	7.66	7.06	5.33	3.65	13.62
D4	415.62	302.42	311.20	256.53	215.05	16.58	10.82	11.01	7.86	5.27	19.13
D5	418.25	306.27	318.17	265.91	220.71	17.52	11.32	11.72	8.52	5.63	17.08
E1	189.82	147.74	139.35	111.00	90.12	10.04	6.84	6.86	5.21	4.25	-26.6
E2	838.78	609.45	578.01	459.79	366.13	10.96	10.12	9.67	8.01	5.57	17.47
E3	648.16	469.00	423.70	310.64	222.40	13.76	12.62	11.81	9.04	5.51	37.94

E4	814.91	602.69	563.67	444.93	348.81	9.81	9.14	8.71	7.23	4.96	19.45
E5	682.48	492.27	451.70	338.23	244.85	17.29	15.57	14.60	11.11	6.79	31.85
E6	285.65	253.66	219.64	177.44	143.05	6.01	5.30	4.34	2.87	1.31	31.54
F1	568.54	432.29	419.13	336.43	276.12	9.60	8.39	7.93	6.15	4.05	22.92
F2	417.57	313.82	288.08	223.95	174.32	15.22	11.79	10.51	7.28	4.53	32.80
F3	593.29	428.33	388.52	292.64	217.07	14.80	13.00	11.96	8.82	5.37	36.51
F4	402.69	306.32	280.64	221.20	170.95	14.74	11.42	10.13	7.12	4.36	32.18
F5	550.78	395.41	372.62	287.31	221.36	15.26	12.79	11.94	8.74	5.53	33.07
F6	850.33	620.04	590.38	469.50	373.29	9.51	8.83	8.45	7.07	4.93	17.11
F7	325.89	266.45	250.78	209.60	172.94	11.30	8.84	7.97	5.85	3.74	18.38
F8	464.81	357.61	339.96	276.95	226.46	15.13	12.10	11.17	8.23	5.36	22.80
F9	547.16	398.35	367.50	281.38	214.69	14.16	12.13	11.19	8.19	5.12	35.82

From Table 2, the minimum and maximum SNR and CNR values were obtained at E1 (Right wrist AP) and D2 (Pelvis AP) and while, the maximum CNR was at E6 (Right elbow AP) and A4 (Skull LAT, right) respectively.

This implies that to be able to visualize an object from the background a higher contrast region, D2 is required. The highest gradient was also recorded at B4 and the minimum value at E1 which implies that to be able to distinguish between different structures of different densities, B4 protocol should be used.

Depending on the SNR, the values recorded for A were lower compared to B, C, D, E and F. The results in Table 3 show that for the labeled region of high contrast numbered from 1 to 5, the SNR was reducing as well as the CNR with the results obtained from D2. The SNR, like the contrast, drops when the difference in attenuation between the object and the background decreases from TG-50. The SNR is proportional to the number of detected radiations, unlike the contrast. Scatter reduces image quality by introducing noise. Object contrast decreases, and the rate of loss is proportional to the object's effective atomic number. As a result, there is a contrast between the air channels (Styrofoam step wedge) and the bony structure (lead step wedge) by differences in attenuation within the phantom. The higher the atomic number of bones, the greater the attenuation coefficient, because the photoelectric cross-section is related to the atomic number increased to the third power. Compton scattering becomes the major interaction activity above 20 keV for soft tissues and beyond 50 keV for bone (assuming the atomic number of bones is 13). The electron density of a material, which varies only minimally with atomic number except for hydrogen, determines the Compton scattering cross section. The electron density of water is comparable to that of bone. As a result, at megavoltage energies, the difference in attenuation, and hence the contrast, is greatly reduced. This explains why CNR readings were observed at lower levels.

Table 3: SNR and CNR values of the irradiated phantom using the FDP

Assigned Label	SNR for Low Contrast Region							CNR for Low Contrast Region							Fitted Line Gradient	
	1	2	3	4	5	6	7	1	2	3	4	6	6	7	A	B
A1	51.57	60.12	70.42	59.21	65.16	70.13	75.47	0.45	0.10	0.69	3.19	3.05	2.59	1.72	41.09	12.97
A2	42.39	58.13	69.24	60.87	67.87	73.97	78.39	8.00	5.80	2.93	6.56	5.81	4.34	1.59	19.23	13.94
A3	38.82	59.21	72.86	62.76	65.72	77.48	83.31	9.52	7.32	4.13	7.73	6.67	4.95	1.49	16.63	16.51
A4	62.21	94.59	127.55	97.94	113.58	127.12	141.36	13.49	9.54	4.95	10.10	8.56	5.79	1.54	24.44	26.10
A5	38.45	53.96	67.02	57.45	63.33	70.11	79.06	7.65	5.66	2.93	6.35	5.53	4.17	1.74	22.42	14.61
A6	41.10	57.75	72.09	61.99	66.16	76.00	82.74	9.17	6.99	3.94	7.42	6.38	4.66	1.52	17.55	16.12
A7	42.01	60.46	72.44	62.54	66.04	75.80	85.02	9.28	7.01	3.95	7.46	6.39	4.58	1.67	17.64	14.47
A8	61.01	78.85	99.28	83.93	93.43	104.11	113.40	8.48	5.64	2.57	6.85	5.87	4.20	1.46	36.71	22.62
B1	76.06	101.23	129.30	110.75	126.04	137.96	158.10	11.62	7.49	3.68	8.33	7.02	4.60	1.45	27.97	15.45
B2	119.47	160.17	200.59	171.30	196.94	211.65	242.26	13.51	6.93	3.11	8.16	6.74	4.07	1.33	30.44	9.78
B3	172.45	148.06	165.16	182.30	204.34	212.07	237.04	10.33	5.44	2.37	6.96	5.76	3.74	1.33	38.61	14.34
B4	69.46	86.06	106.66	87.95	97.71	108.82	117.92	3.13	1.74	0.39	4.46	4.18	3.24	1.82	22.12	49.18
B5	159.47	180.21	197.14	216.08	231.71	239.63	244.44	3.43	1.80	0.48	4.88	4.37	3.20	1.62	7.09	5.58
B6	114.33	152.42	186.01	158.11	181.54	194.93	220.79	13.03	6.92	3.10	8.04	6.58	4.10	1.20	35.32	13.92
B7	167.44	196.32	210.40	206.05	225.11	231.22	237.18	9.85	5.56	2.40	7.23	6.11	4.13	1.69	15.93	7.34

C1	77.03	116.13	143.27	122.90	133.73	151.59	161.36	14.29	9.57	4.83	10.45	8.44	5.71	1.44	20.50	18.35
C2	222.81	300.18	357.00	310.90	356.04	382.55	409.29	14.14	7.68	3.54	9.66	7.87	4.98	1.51	-3.51	-0.94
C3	72.43	100.59	120.75	104.30	118.75	132.24	142.67	10.56	6.72	3.13	7.91	6.60	4.56	1.41	35.56	21.06
C4	87.17	115.31	133.65	119.55	135.89	145.22	155.90	10.86	6.67	3.05	8.02	6.63	4.49	1.40	30.43	17.59
C5	75.38	108.48	133.68	113.24	127.21	141.43	152.07	12.62	8.25	4.16	9.17	7.51	5.09	1.39	25.90	30.04
C6	77.07	110.46	134.81	115.64	128.35	142.21	155.04	13.13	8.60	4.29	9.50	7.74	5.21	1.45	26.04	19.42
C7	105.51	112.52	118.48	104.23	110.44	118.08	123.04	0.95	1.22	1.43	3.44	3.19	2.66	1.78	-8.22	12.32
C8	77.56	111.72	138.35	117.26	131.87	146.51	158.42	13.93	9.11	4.66	10.06	8.26	5.56	1.53	23.97	8.53
C9	62.75	88.56	118.18	91.91	107.93	120.30	133.82	11.64	8.17	4.08	8.73	7.44	5.06	1.31	34.21	27.67
C10	91.50	125.23	148.84	129.46	146.80	158.27	167.86	12.95	8.15	4.03	9.25	7.57	5.11	1.54	22.14	15.55
D1	87.24	103.92	117.05	114.25	125.50	137.12	142.67	3.76	1.86	0.69	4.69	4.02	3.06	1.56	39.58	15.73
D2	224.80	302.05	342.90	307.15	352.85	378.91	408.98	14.21	7.70	3.60	9.68	7.84	4.96	1.47	-0.39	-1.17
D3	97.84	118.35	129.77	129.97	141.41	150.94	154.97	6.44	3.51	1.55	5.75	4.75	3.49	1.54	29.96	13.30
D4	82.62	102.79	114.66	110.30	122.33	129.68	139.55	5.16	2.78	1.18	5.01	4.26	3.14	1.45	43.78	18.06
D5	102.72	141.96	165.54	146.39	159.87	176.96	177.62	13.61	8.58	4.54	9.71	7.75	5.39	1.83	17.18	13.85
E1	30.83	43.62	51.74	46.77	49.51	54.94	60.53	8.04	6.13	3.40	6.50	5.59	4.14	0.81	10.02	10.57
E2	123.20	163.56	198.19	170.01	193.45	209.25	230.33	14.54	7.86	3.40	8.83	6.93	4.29	1.24	32.73	14.00
E3	49.31	70.13	97.29	72.40	86.01	97.60	114.25	8.66	6.04	2.69	7.05	6.06	4.41	1.62	50.66	28.73
E4	115.08	154.18	186.47	157.42	183.86	196.91	218.90	12.55	6.76	2.90	7.82	6.25	3.89	1.18	35.97	14.24
E5	55.43	79.24	113.01	82.47	99.56	113.34	129.55	11.89	8.71	4.46	9.06	7.71	5.26	1.52	33.59	26.98

E6	126.63	128.03	134.21	101.43	110.65	115.93	119.18	1.56	1.65	1.87	3.34	3.18	2.77	2.08	0.76	9.35
F1	104.31	135.74	161.11	143.05	160.50	171.15	181.51	9.03	4.93	2.05	6.49	5.17	3.44	1.26	37.42	19.21
F2	56.14	74.97	93.14	77.75	90.71	97.23	106.31	7.61	5.06	2.23	6.24	5.42	3.98	1.63	38.89	21.31
F3	57.88	80.06	104.12	86.09	96.79	108.96	121.89	9.17	6.23	2.76	7.34	6.30	4.47	1.67	45.94	26.49
F4	56.15	74.85	91.60	76.76	89.66	94.00	103.68	7.23	4.78	1.99	6.03	5.26	3.88	1.67	21.72	41.57
F5	62.73	88.13	109.68	89.88	104.75	116.19	128.68	10.46	7.22	3.55	7.71	6.38	4.31	1.33	39.73	26.81
F6	117.76	160.16	199.05	166.68	193.20	213.19	231.47	12.72	6.46	2.74	8.19	6.38	4.10	1.33	30.82	11.62
F7	74.12	90.97	107.10	96.52	109.89	113.85	119.98	6.92	4.27	1.76	5.49	4.67	3.30	1.35	37.55	19.68
F8	83.15	106.45	131.01	113.17	124.11	138.83	150.44	11.14	7.21	3.30	8.06	6.55	4.48	1.47	33.07	19.17
F9	60.22	83.28	104.98	85.75	100.75	107.13	124.81	9.50	6.49	3.16	7.04	5.84	3.87	1.28	44.43	28.55

From Table 3, the maximum SNR was recorded at C2 (T-spine AP) and the minimum value at E1 (Right wrist PA), while the maximum value of CNR was recorded at A4 (Skull LAT, right) and the minimum at E1 (Right wrist PA), and this was similar for the high contrast region. This implies that to be able to visualize tissue from a background, C2 (T-spine AP) is required. The SNR gives the uniformity of the fall within a particular area, thus, the highest SNR and CNR give a clearer image. Also, the highest gradients were recorded at B4 (Right clavicle AP axial) and E3 (Right shoulder AP) and the lowest values were at D2 (Pelvis AP) and C7 (L spine AP). As a result, there was noise in the D2 (Pelvis AP) image, making it not possible to see the image from the background, whereas A4 (Skull LAT, right) gave a clearer image.

The highest gradients were recorded for the two Styrofoam step wedges of different density implies that to be able to distinguish between structures of different densities in the low contrast region, E3 (Right shoulder AP) protocol should be selected, likewise B4 (Right clavicle AP axial) in the high contrast region.

This also implies that to be able to distinguish between different densities or structures, B4 and E3 should be used. Depending on the SNR, the values recorded for A were lower compared to B, C, D, E and F for the low contrast region also. The results in Table 3 show that, for the labeled region of low contrast numbered from 1 to 7, the SNR decreased from region 1 to 3 and then from region 4 to 7 for the two-step wedges of different thickness, as well as CNR. The best results were obtained at C2. There were two gradients for the low contrast because of the two-step wedges of different thickness representing the low contrast region. The maximum gradient was recorded at B4 and E1.

From the analyses, the optimal image quality was obtained with 70 kVp and 8 mAs (Skull Lat), but for better visualization of a soft tissue, it is prudent to use 65 kVp and 16 mAs (Right Clavicle AP). CNR less than five indicates the images are not of good quality and that it is difficult to resolve two regions of clinical interest.

For resolution of the images, 1-mm patterns of aluminum used could not be resolved after imaging. However, 2-mm and 3-mm patterns of aluminium were able to be resolved.

Conclusion

This study has verified and demonstrated the feasibility of using a digital flat panel detector (FPD), originally designed for conventional diagnostic x-ray radiography, for patient setup verification with a cobalt-60 teletherapy machine. Despite the detector's reliance on pre-defined exposure parameters tailored to diagnostic anatomical regions and x-ray tube settings, it was successfully adapted to work with the monoenergetic megavoltage cobalt-60 beam, producing high-quality portal images.

Notably, the pre-defined exposure presets available in the detector were found to enhance image quality even under cobalt-60 beam conditions. For instance, selecting the "Pelvis AP" protocol resulted in improved visualization of bony landmarks, while "Shoulder AP" settings provided superior imaging for lung regions, which is relevant for breast irradiation verification.

Image quality was quantitatively assessed using key digital imaging performance indicators: Signal-to-Noise Ratio (SNR) and Contrast-to-Noise Ratio (CNR). The results confirmed that the adapted FPD system can deliver clinically acceptable image quality for positional verification.

As Electronic Portal Imaging Devices (EPIDs) play a critical role in ensuring patient positioning accuracy during radiotherapy, it is recommended that the performance of flat panel detectors be routinely evaluated. Clinics incorporating such systems should also establish strict quality assurance protocols to maintain imaging reliability and treatment precision.

Acknowledgements

The authors wish to thank the UG Tullow Scholarship Scheme for funding this research work.

References

[1] AAPM Radiation Therapy Committee Task Group 58. Med Phys. 2001;28(5):712–737. doi:10.1118/1.1369626

[2] Dieterich, S., Ford, E., Pavord, D., & Zeng, J. (2016). In-Vivo Dosimetry. *Practical Radiation Oncology Physics*, 30–39. https://doi.org/10.1016/B978-0-323-26209-5.00003-1

[3] Ebert, N., Tillner, F., & Baumann, M. (2018). Radiation oncology. *Encyclopedia of Cancer*, 321–336. https://doi.org/10.1016/B978-0-12-801238-3.65428-4

[4] I.A.E.A Human Health reports, N. 7. (2013). Record and Verify Systems for Radiation Treatment of Cancer: Acceptance Testing, Commissioning and Quality Control. *Number 7*, 39. http://www-pub.iaea.org/MTCD/Publications/PDF/Pub1607_web.pdf

[5] Ebert, N., Tillner, F., & Baumann, M. (2018). Radiation oncology. *Encyclopedia of Cancer*, 321–336. https://doi.org/10.1016/B978-0-12-801238-3.65428-4

[6] Herman, M. G., Balter, J. M., Jaffray, D. A., McGee, K. P., Munro, P., Shalev, S., Van Herk, M., & Wong, J. W. (2001). Clinical use of electronic portal imaging: Report of AAPM Radiation Therapy Committee Task Group 58. *Medical Physics*, *28*(5), 712–737. https://doi.org/10.1118/1.1368128

[7] I.A.E.A Human Health reports, N. 7. (2013). Record and Verify Systems for Radiation Treatment of Cancer: Acceptance Testing, Commissioning and Quality Control. *Number 7*, 39. http://www-pub.iaea.org/MTCD/Publications/PDF/Pub1607_web.pdf

[8] Olaciregui-Ruiz, I., Beddar, S., Greer, P., Jornet, N., McCurdy, B., Paiva-Fonseca, G., Mijnheer, B., & Verhaegen, F. (2020). In vivo dosimetry in external beam photon radiotherapy: Requirements and future directions for research, development, and clinical practice. *Physics and Imaging in Radiation Oncology*, *15*(March), 108–116. https://doi.org/10.1016/j.phro.2020.08.003

[9] Tsutomu, G., Kichirou, K., Tosiaki, M., Jun, M., & Hiroshi, H. (2006). *An Experiment Comarison of Flat-Panel Detector performance For Direct and Indirect Systems(Initial Experiences and Physical Evaluation)*. *19*, 362–370.

[10] van Elmpt, W., McDermott, L., Nijsten, S., Wendling, M., Lambin, P., & Mijnheer, B. (2008). A literature review of electronic portal imaging for radiotherapy dosimetry. *Radiotherapy and Oncology*, *88*(3), 289–309. https://doi.org/10.1016/J.RADONC.2008.07.008